



Enhanced photocatalytic reactions via plasmonic metal-semiconductor heterostructures combining with solid-liquid-gas interfaces

Shan-Jiang Wang^{a,b}, Xiao-Yang Zhang^{a,b}, Dan Su^{a,b}, Xi Yan^a, Huan-Li Zhou^a, Xiao-Mei Xue^b, Yun-Fan Wang^a, Tong Zhang^{a,b,*}

^a Joint International Research Laboratory of Information Display and Visualization, School of Electronic Science and Engineering, Southeast University, Nanjing 210096, People's Republic of China

^b Suzhou Key Laboratory of Metal Nano-Optoelectronic Technology, Southeast University Suzhou Campus, Suzhou, Jiangsu, 215123, People's Republic of China

ARTICLE INFO

Keywords:

Water treatment
Plasmonic metal-semiconductor heterostructures
Separation of electron-hole pairs
Solid-liquid-gas triphase
Dissolved oxygen

ABSTRACT

Photocatalytic water pollution remediation is currently a hot issue in the field of environmental protection. However, the limited optical adsorption, recombination of electrons and holes, as well as low kinetics in solid-liquid conditions impede the further improvement in photoactivity. Inspired by the degradation mechanism of photocatalytic process, started with interfacial engineering, in this paper, plasmonic metal-semiconductor heterostructures (PMSHs) combined with an optimized dissolved oxygen transporting channel were prepared. With the synergetic help of PMSHs and superhydrophilic-superhydrophobic (superwetting) reaction interface, it is not only can realize the effective capture of photons in the visible light band, but also promote the fully separation of electron-hole pairs. The efficiency in PMSHs based triphase system is ~60 times higher than traditional solid-liquid system, and is ~3 times higher than PMSHs based solid-liquid system. The stability and wide applicability in series organic dyes degradation also made it a good potential for practical pollutants water treatment.

1. Introduction

Environmental pollution problems, especially water pollution, have always been a hot topic due to highly dependent on water resources for human lives [1,2]. In all pollutants water treatment schemes, photocatalysis is deemed to be a cost-effective way to solve the problems thoroughly which could be driven by clean and reproducible solar energy, and thus there are tremendous efforts have been made to achieve regeneration of clean water globally [3–5]. Semiconductor based photocatalysts, such as TiO₂, ZnO, etc., have been discovered to be excellent medias owing to their matched redox potentials, strong ability to supply electron-hole pairs, instinctive biocompatibility, structural stability and abundant of raw materials [6–10]. Especially, commercial P25 consist of TiO₂ (anatase: rutile = 4: 1) with mean size of 25 nm has always been applied at daily lives and industry owing to its superior photoactivity, physicochemical stability and low-cost. Most of the semiconductor based photocatalysts studied, however, can only be activated by the photons within the bandgap, eg. TiO₂ could be activated only by light in UV range, which lead to greatly waste of energy with longer range of

light in the whole solar spectrum. Meanwhile, the limit of separation efficiency of generated electron-hole pairs due to defects and grains presented could also cause the decrease of catalytic activity. To avoid these core problems, many pioneer works including deposition of metal nanoparticles [11], transition metal and non-metal doping [12,13], semiconductor heterostructure formed [14] and structural defects construction [15] in order to achieve enhancement of photocatalytic efficiency were proposed in past years. All these routes provided reliable ways for enhancing photoactivity beginning with crystal growth theory and basic photocatalytic mechanism.

Plasmonic metal-semiconductor heterostructures (PMSHs) mediated photocatalysts based on hot-electron effect have attracted tremendous attentions in near recent years for their breakthrough in limits of bandgap in conventional semiconductor based photocatalysts [16–18]. Taking plasmonic metal (Au or Ag) as an example, when irradiated by visible light, hot-electrons were excited by intraband transition process from whose electrons located at filled s band leap into empty sp band above the Fermi level, and then inject into conduction band of formed n-type semiconductors and promote the redox reactions. The behaviors

* Corresponding author at: Joint International Research Laboratory of Information Display and Visualization, School of Electronic Science and Engineering, Southeast University, Nanjing 210096, People's Republic of China.

E-mail address: tzhang@seu.edu.cn (T. Zhang).

<https://doi.org/10.1016/j.apcatb.2022.121102>

Received 9 October 2021; Received in revised form 4 January 2022; Accepted 14 January 2022

Available online 18 January 2022

0926-3373/© 2022 Elsevier B.V. All rights reserved.

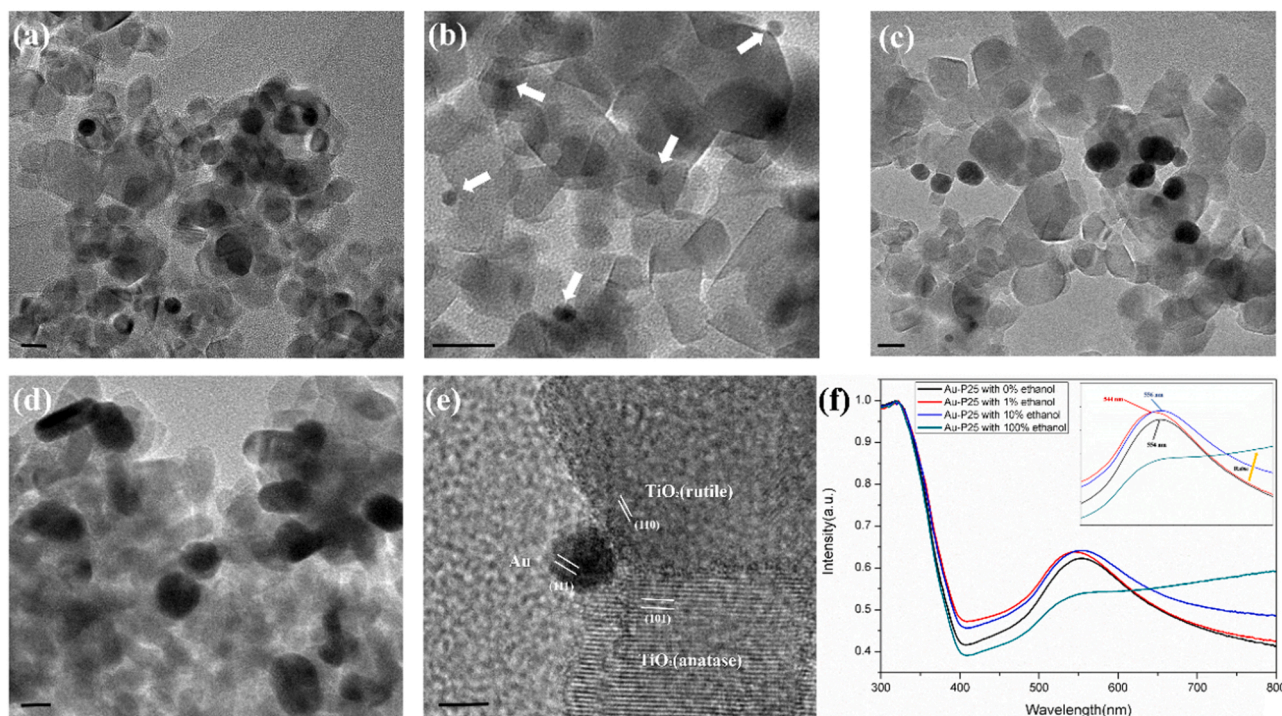


Fig. 1. The TEM images of Au-P25 with (a) 0% v/v ethanol, (b) 1% v/v ethanol, (c) 10% v/v ethanol and (d) 100% v/v ethanol. (e) HRTM of Au-P25 with 1% ethanol. (f) The corresponding results of adsorption spectra. Scale bars in panels a-d are 10 nm; Scale bars in panel e is 5 nm.

of these energetic electrons are sensitive to the morphology, composition and surroundings of plasmonic nanostructures [16,18,19]. Relevant works have been reported for how to design and prepare PMSHs with high photoactivity for solar energy conversion application [19,20]. However, the current methods still require complex crystal growth routes to adjust the morphology and quality of crystal, post-processing to eliminate the influence of template or protective agent, and practical bottlenecks of difficult to mass-produce [21–23]. Therefore, to achieve controllable and efficient light absorption and hot-electrons transportation, it is necessary to find a reliable pathway with mass-capable to achieve carefully photons capture and charges separation. Among all the routes for preparation of PMSHs, photochemical reduction is considered to be a green, fast and reproducible method by only adjusting metal sources, light intensity and wavelength [24–26]. Despite many efforts made before, the relationship between morphology and effective charges separation is still needed to be revealed clearly due to difficulty in control of reaction rates. Electron or hole scavenger which was used usually in mechanism explanation of catalytic reactions [27–29] also played a key role in deposition rates of plasmonic nanostructures which could be prepared with better crystal quality and morphology control.

Most of PMSHs were designed by interfacial engineering which aiming at optimization of photons trapping mechanism and electrical transporting channels at nanoscale. However, most of these works were usually considered under the condition of conventional solid (PMSHs)-liquid (pollutants water) diphasic catalytic system. In terms of basic mechanism, reactive oxygen species (ROS), such as singlet oxygen ($^1\text{O}_2$) and superoxide anion ($\text{O}_2^{\bullet-}$) with strong redox activity, are deemed to play the key role in the photocatalytic reaction system [30,31]. Furthermore, the crucial ROS was mainly determined by the contents of dissolved oxygen in water-based reaction system. In this process, ROS was produced by removing generated electrons at the surface of catalysts with the help of dissolved oxygen. However, oxygen is always insufficient in water compared to air reaction system. Especially, once redox reaction is mediated under high-light density or photocatalysts with excellent capacity of generation of electron-hole pairs, the balance

of oxygen supply and oxygen consumption would be broken down and thus the rates of catalytic reaction would be suppressed and then decrease the efficiency in whole system. To solve this problem, pioneer works considering a solid-liquid-gas triphase system by introducing superwetting membrane constructed with superhydrophilic active sites and superhydrophobic support were presented in near recent years [32–35]. In such system, the enhancement of O_2 concentration has been realized directly and shortly by interfacial O_2 injection benefited from such special wetting properties of membrane. This triphase system has been applied in many fields including water pollution treatment [36, 37], bioassay system [38] and renewable energy production [39].

Inspired by the essence of photocatalytic reaction, in this work, a plasmonic metal-semiconductor heterostructures (PMSHs) combined with a solid-liquid-gas triphase photocatalytic system was reported for the first time. In this system, superhydrophilic plasmonic Au-P25 and superhydrophobic PTFE-modified carbon black were used for contribution of triphase system. Au-P25 was synthesized by ethanol assisted photochemical reduction process. Relationships of size, shape and distribution for loaded Au NPs were investigated by addition of different volumes ethanol, photocatalytic results in diphasic system and photocurrent measurements demonstrated the photoactivity evolution versus morphology control. Then, improvement of the degradation efficiency for organic pollutants in triphase system was demonstrated by making comparison with conventional solid-liquid diphasic system with PMSHs or not. The key factors of dissolved oxygen were studied and the corresponding explanation is also given in details. Finally, experimental investigation of the material photostability with tens of test cycles and broad practicability by degrading series of dyes were also included.

2. Experimental section

2.1. Reagents

Chloroauric acid hydrated ($\text{HAuCl}_4 \cdot x\text{H}_2\text{O}$), potassium iodide (KI), copper (II) chloride dehydrate (CuCl_2), p-Benzoquinone (PBQ), L-Tryptophan (L-Tr), isopropyl alcohol (IPA) and anhydrous ethanol was

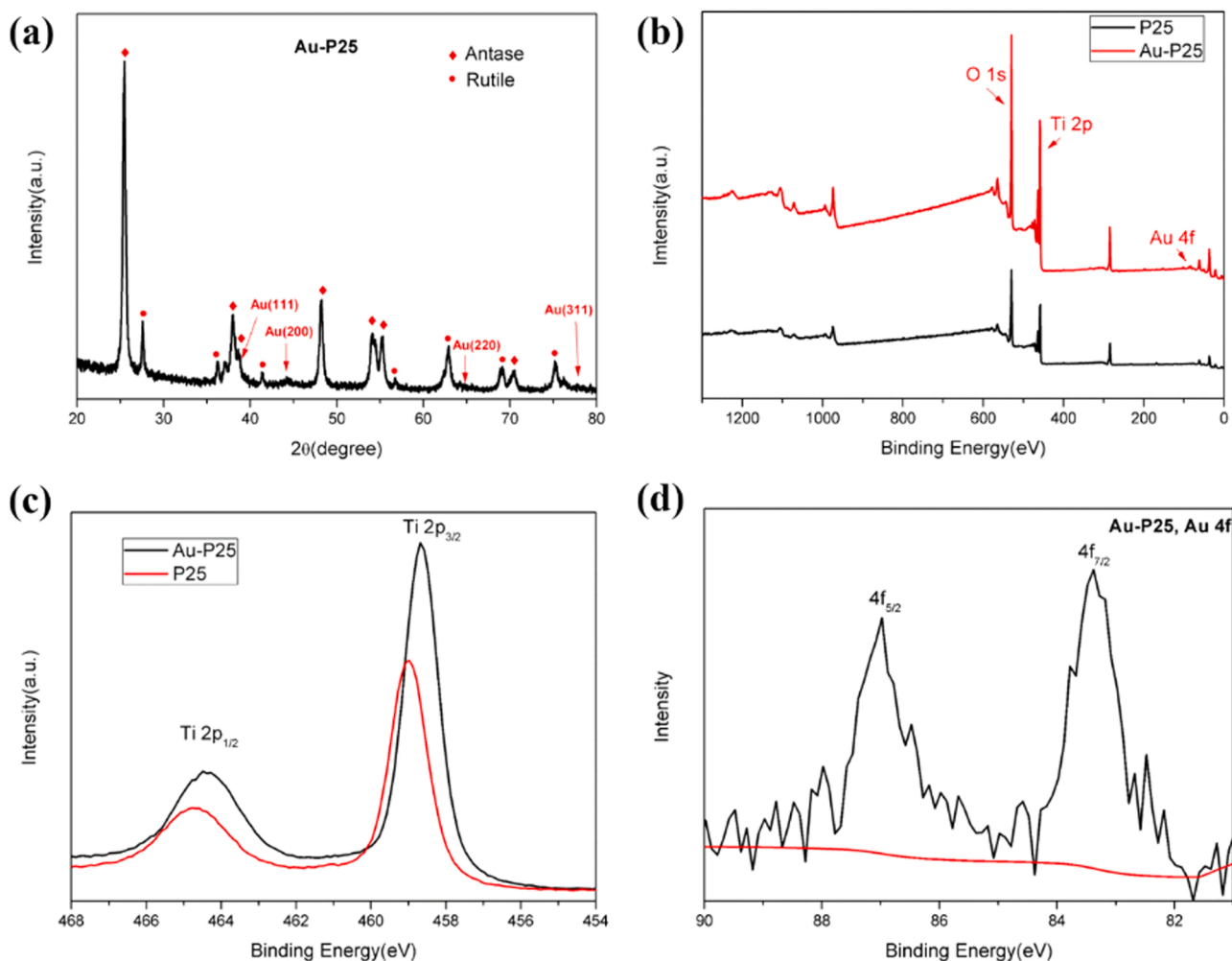


Fig. 2. (a) XRD spectra, and (b) XPS survey spectra of P25 and Au-P25. High resolution XPS spectra of Ti 2p core level (c) and Au 4f core level (d).

purchased from Sigma-Aldrich (Shanghai, China). P25 (TiO₂, anatase: rutile = 4: 1, Degussa) was obtained from Merck (Germany). Salicylic acid (SA), Methylene blue (MB), rhodamine B (RhB), methyl orange (MO) and rhodamine 6 G (R6G) were bought from Aladdin (Shanghai, China). Superhydrophobic membrane with a PTFE modified carbon black (29 BCE) was obtained from Gaosunion. Degassing distilled water (18.2 MΩ·cm) was used in all experiments. All the chemicals were analytical grade and used without further purification.

2.2. Preparation of plasmonic heterostructures

Au-P25 photocatalysts were prepared by the following process: P25 (10 mg) ultrasonic dissolved in the distilled water (10 mL) containing HAuCl₄·xH₂O (0.1 mL, 1 mM). After that anhydrous ethanol with calculated volumes was dropped and uniformly dispersed by hand-shaken. The reaction solution was put under the home-made UV lamp (12 W, 365 nm) for 10 min. The photocatalysts were recovered by centrifugation, washed and dried at 333 K for 6 h. The additives were increased in proportion for gram-scale photocatalysts preparation without any modifications. Finally, the photocatalysts were dispersed to the mixture of 1:1 ethanol/water (vol), then were filtering coated to 1 cm × 3 cm PTFE modified carbon black to achieve the superwetting photocatalytic membrane for solid-liquid-gas triphase photocatalytic system and to 1 cm × 3 cm glass for conventional solid-liquid diphas photocatalytic system.

2.3. Quantification of photocatalytic H₂O₂

Ghormley triiodide method was used to determine the generation of photocatalytic H₂O₂. Specifically, in this method, I₃⁻ was used as a typical analyte which could be measured at the absorbance of 360 nm after oxidation of I⁻ to I₃⁻ in the presence of H₂O₂. A linear correlation between the I₃⁻ absorbance and standard H₂O₂ solution with known concentration (0.1–500 μM) could be acquired by a calibration curve. For the quantification of standard H₂O₂ solution, 0.2 mL standard H₂O₂ solution, 0.1 mL of 1 M KI, 0.1 mL of 1 M HAc/NaAc, and 1.6 mL of H₂O were mixed and then stirred to obtain a homogeneous solution. Next, the mixed solution was left undisturbed for at least 5 min until complete reaction and then for absorbance measurement at 360 nm. For the quantification of generated photocatalytic H₂O₂ in the diphas and triphase system both for P25 and Au-P25. 300 W Xe lamp (λ > 400 nm) was used as the light source, the incident photonic flux was monitored by a photometer during the experiments. The reaction process was brought in a cuvette (other parameters were the same as previous quantification of standard H₂O₂ solution) and measuring the absorbance at fixed intervals.

2.4. Photocatalytic Degradation of organic dyes

Organic dyes with initial concentrations of 20 mg L⁻¹ for SA and 10⁻⁵–5 M for MB, RhB, MO and R6G were used for series of model organic pollutants to be degraded. A 300 W Xe lamp (λ > 400 nm) was used for light source for visible-light photocatalysis. For the triphase

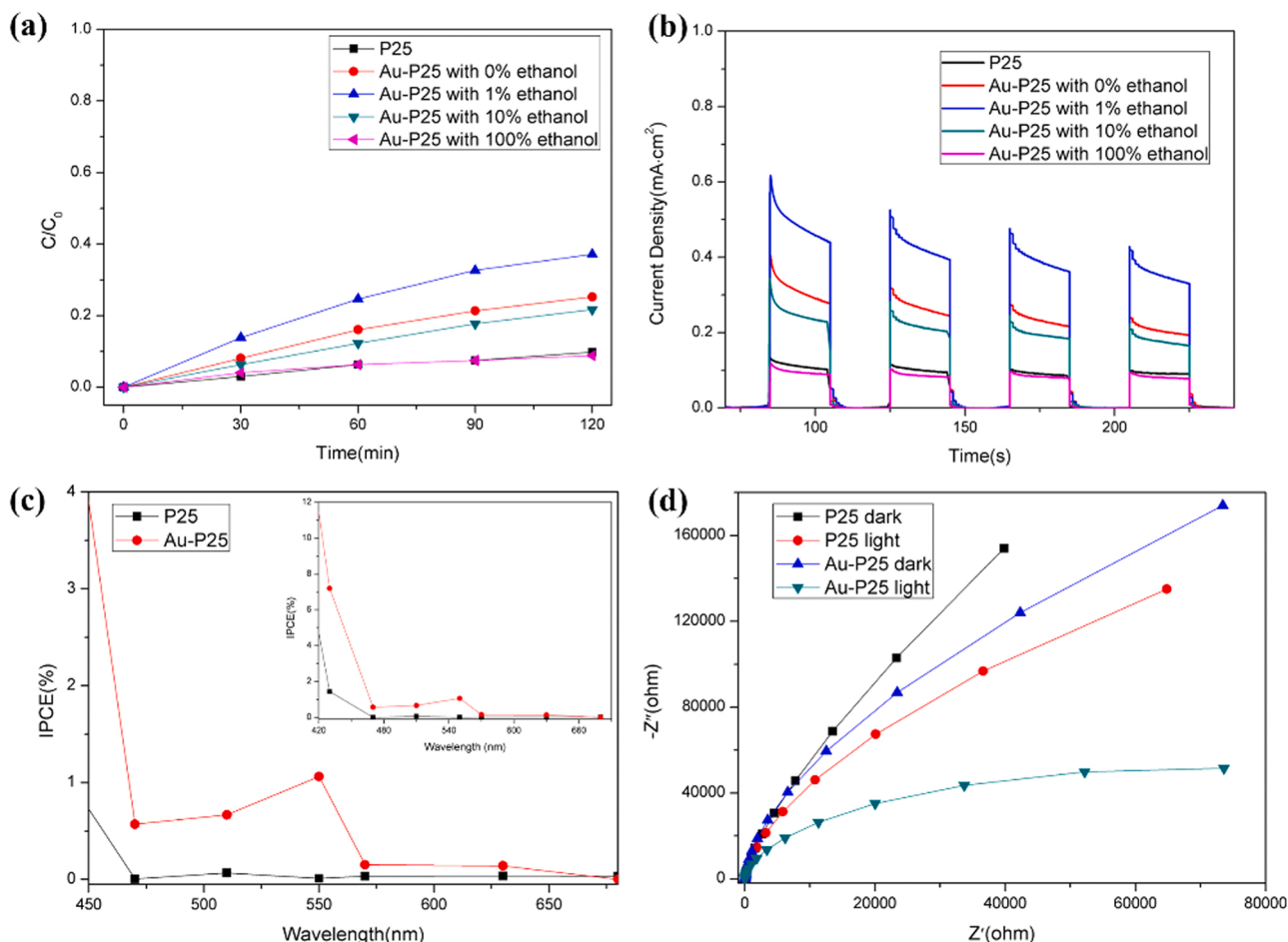


Fig. 3. The activity of photocatalyst in diphasic system (a) and corresponding measurements of photocurrents curves (b). (c) IPCE and (d) EIS measurements of P25 and Au-P25 with 1% ethanol under visible light illumination.

photocatalytic system, the membrane was vertically inserted into the water by the means of semi-immersion which the area of coated photocatalysts was contacted with water and other area was exposed to air. For the diphasic photocatalytic system, the coated glass was immersed into water thoroughly. Before the irradiation of light, all the reaction systems were placed without disturbed under dark condition for at least 1 h to reach the adsorption-desorption equilibrium. The rates of dyes degradation were detected by UV-vis absorption spectrum after intervals of irradiation (0, 30, 60, 90 and 120 min). The final efficiency (%) was calculated by the formula as followings,

$$(C_0 - C)/C_0 \times 100\% = (A_0 - A)/A_0 \times 100\%$$

Where C_0 and A_0 were the initial concentration and absorbance of dyes, respectively, C and A were the remaining concentration and absorbance of dyes, respectively.

2.5. General characterization

Morphologies of the photocatalysts were investigated by transmission electron microscope (TEM, Zeiss Sigma 300, Germany) and scanning electron microscope (SEM, Zeiss Sigma 300, Germany). Optical analysis was recorded by the UV-vis absorption spectra (PE lambda 750, USA). Structure information was observed by X-ray photoelectron spectroscopy (XPS, Thermo Alpha, USA). The contents of the target element were monitored by inductively coupled plasma-optical emission spectroscopy (ICP-OES, PerkinElmer 8300, USA). Contact angles were measured more than three different positions by using a contact angle measurement system (JY-82B Kruss DSA, Germany). The detection

of generated ROS was carried out by electron paramagnetic resonance (EPR, Bruker EMXplus, Germany). 5,5-dimethyl-1-pyrroline N-oxide (DMPO) methanol solution, DMPO aqueous solution, 2,2,6,6-tetramethyl-1-piperidine (TEMP) and 2,2,6,6-tetramethylpiperidine-1-oxyl (TEMPO) were used as agents for superoxide radical ($\cdot\text{O}_2^-$), hydroxide radical ($\cdot\text{OH}$), singlet oxygen ($^1\text{O}_2$) and hole (h^+) trapping experiments. The photocurrents were measured by an electrochemical workstation (CHI660C Instruments) with a standard three-electrode system using Ag/AgCl electrode, Pt wire and ITO as reference, counter and working electrodes, respectively. Na_2SO_4 solution (0.5 M) was used as electrolyte. A 300 W Xe lamp ($\lambda > 400$) nm was used as the light source and a bias was set to 0.5 V. For incident photon-to-current conversion efficiencies (IPCE) measurement, the sample was irradiated by a series of monochromatic light by adding specific filters in front of the Xe lamp. The power of the incident light of each wavelength and the corresponding photocurrent was measured to evaluate IPCE. Electrochemical impedance spectroscopy (EIS) measurement was performed over a frequency range of $0.1\text{--}10^5$ Hz with an AC amplitude of 10 mV.

3. Results and Discussion

Scheme A showed the principal diagram of the PMSHs-mediated solid-liquid-gas triphase photocatalytic system. The catalytic membrane was divided into two sections, one is superhydrophilic active sites which direct contact with pollutants water, and another one is superhydrophobic surface acted as O_2 storage and transporting support exposed to surrounding air. Superhydrophilic active sites were constructed by plasmonic Au-P25 and superhydrophobic surface was

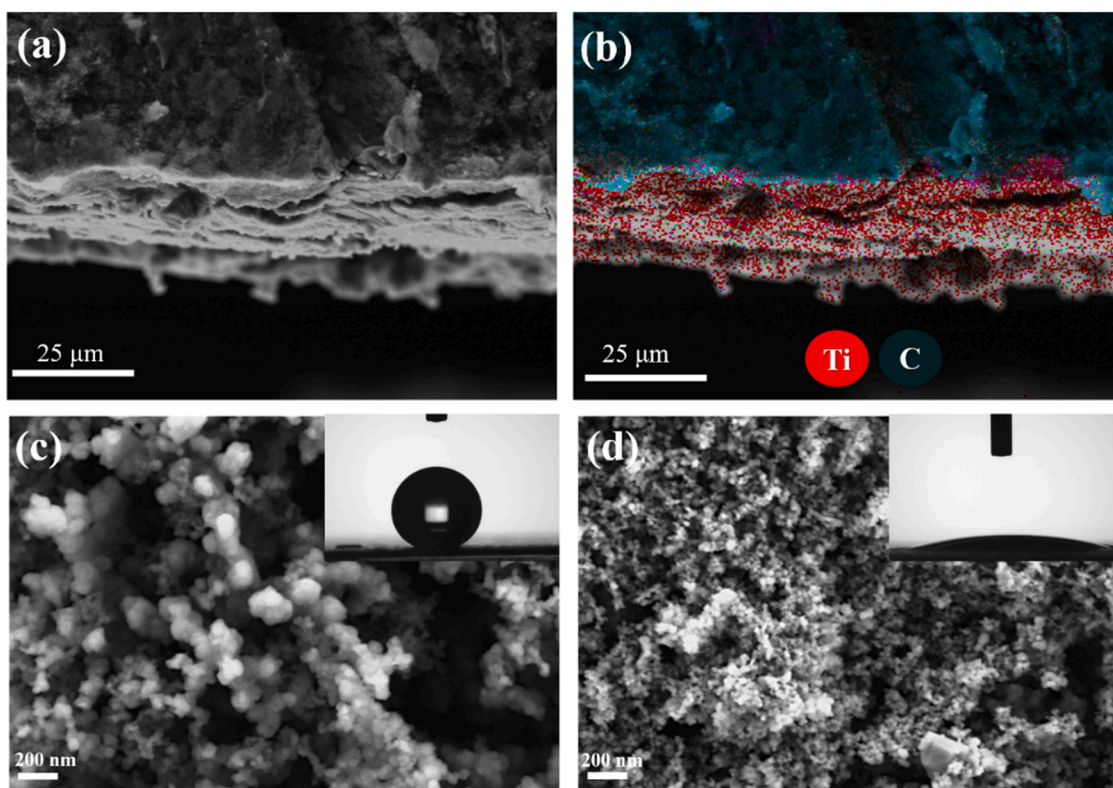


Fig. 4. SEM images (a) and X-ray spectroscopy (b) of superwetting membrane. The enlarged SEM images at superhydrophobic carbon black (d) and superhydrophilic photocatalysts (c), respectively. Inset showed the measurements of CA at different areas.

obtained by PTFE modified porous carbon black. In the photocatalytic process, dissolved oxygen in pollutant water participated in ROS generation by reacting with photogenerated electrons at the hydrophilic surface of catalysts. With the extension of time for catalytic degradation, the reduced oxygen contents were supplemented by stored O_2 in porous superhydrophobic carbon black. Meanwhile, the pores in carbon black were interconnected between water and outside surroundings where water could not penetrate into. Therefore, a dissolved oxygen pathway built up by pollutant water-interfacial photocatalysts-porous carbon black-outside air was realized. The interface with contrast properties built up a fast and short dissolved oxygen pathway. O_2 captured by pores of superhydrophobic carbon black where water could not penetrate into was transported immediately to the surface of solid photocatalysts once consumption of O_2 was taken place in the water. The shorten in distance and uninterrupted supply of O_2 make the key ROS become abundant which then directly affects the rates of photocatalysis.

Scheme B showed the routes for constructing PMSHs-mediated solid-liquid-gas triphase photocatalytic system. Firstly, PMSHs were prepared by photochemical reaction process. Degussa P25 is used as main part of photocatalyst. Chloroauric acid and anhydrous ethanol are used as metal source and hole scavenger, respectively. Briefly, under the illumination of UV light, electron-hole pairs were generated in P25 and separated by rutile phase and anatase phase [40]. Due to abundant oxygen vacancies at the surface of rutile phase where they served as feasible nucleation sites [41], plasmonic metal nanoparticles were formed preferentially on the rutile phase of P25. The Size, shape and distribution of plasmonic Au NPs were controlled by a hole scavenger. Next, the superwetting membrane with superhydrophilic and superhydrophobic interface was fabricated by a simple filtering route, the addition of ethanol would decrease the surface energy of superhydrophobic carbon black and then enhanced the adhesive ability of photocatalysts and loading uniformity.

3.1. Characterization of as-prepared plasmonic heterostructures

The TEM images clearly showed the tendency of size and distribution of Au NPs with different ratio of anhydrous ethanol. Size and density of Au NPs were increased both with the increase of volume of ethanol, as shown in Fig. 1b-d. And Au NPs with irregular shapes were formed when excessive addition of anhydrous ethanol due to promotion of rate of reaction. In contrast, Shape and distribution of Au NPs were uniform similar with 1% v/v% anhydrous ethanol in Fig. 1b. But the size of Au NPs in Fig. 1a were much larger. Fig. 1e and Fig.S1 showed the high-resolution TEM of Au-P25 from Fig. 1b and corresponding spatial elemental distribution. It could be seen that the Au NP is located at the interface of rutile/anatase phase due to relative higher activity [41]. The relationship between distribution and size was also studied in Fig. S2, in the ethanol-promoted process for Au NPs formation, Au NPs migrated as size increased and finally located at the interface, HRTEM (Fig. S3) and corresponding XPS (Fig. S4) analysis confirmed this. The absorption spectra also showed such differences observed in TEM image. Commercial P25 rarely has light absorption in the visible light range, which was in contrast with P25 loaded with different amounts of Au NPs. Compared to Au-P25 with 0% v/v% ethanol, a blue shift of peak showed in Au-P25 with 1% v/v% meant a much smaller size of formed Au NPs. However, the size of Au NPs increased when more ethanol was added, which exhibited a red shift of the peak. Especially, the Au-P25 with 100% v/v% showed a remarkable elevation in a long-wavelength range which resulted from aggregation and shape difference of Au NPs (inset of Fig. 1f). ICP analysis was used to examine the reaction kinetics by monitoring the concentration of Au^{3+} during this entire photochemical process. The final loading amounts of Au ($1.05\% \pm 0.04$) were the same in all samples (Table S1), but Au-P25 with no ethanol addition needed a longer time to complete reaction, and the deposition rates would be enhanced as much more ethanol involving in the reaction (Fig. S5).

The crystal structure of Au-P25 was further investigated by XRD and

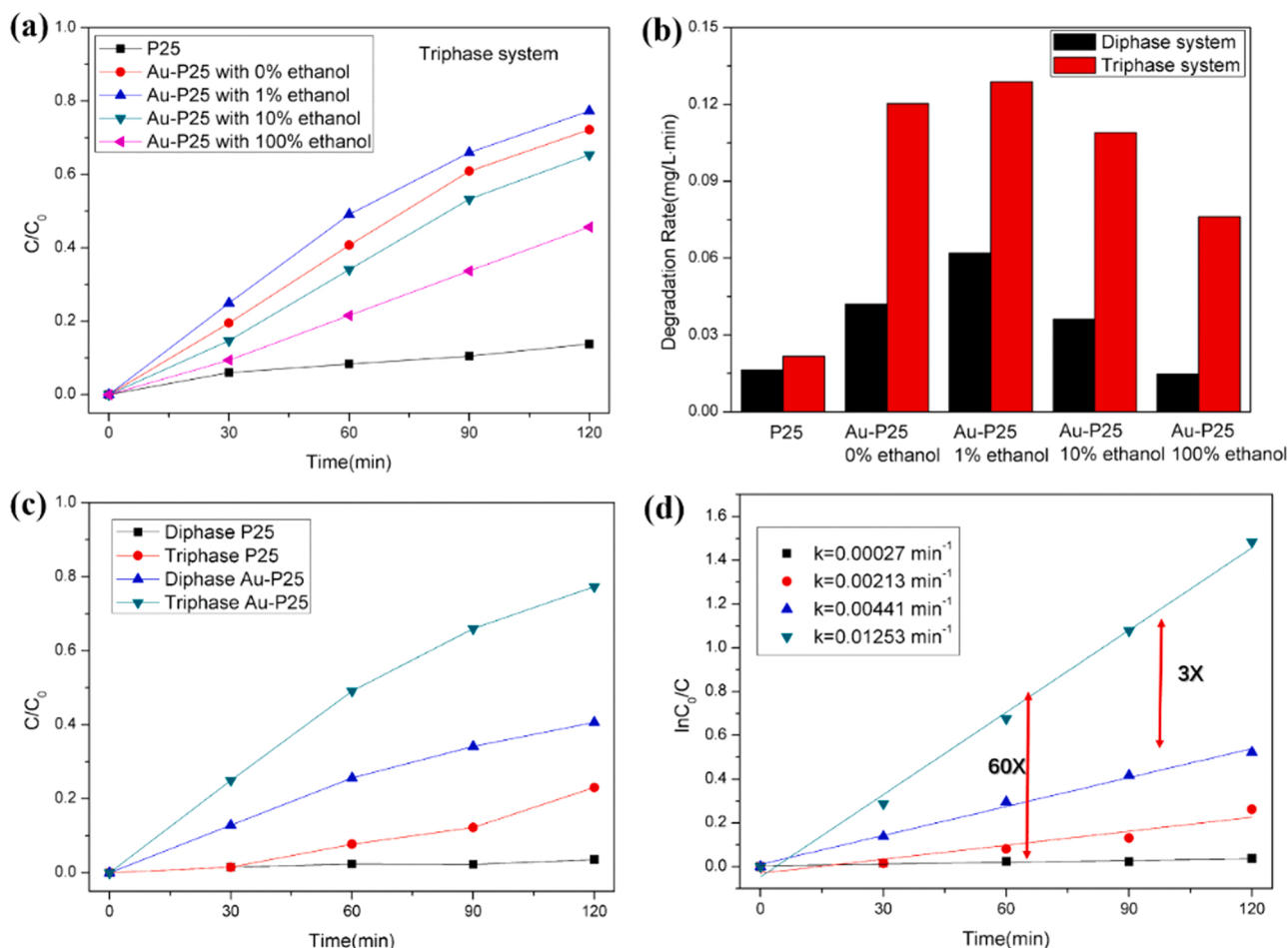


Fig. 5. The activity of photocatalysts prepared with different volumes of ethanol in triphase system (a) and corresponding comparisons in diphasic and triphase systems (b). The SA degradation efficiency of Au-P25 with 1% ethanol and P25 in diphasic system and triphase system, respectively (c), and corresponding reaction rate curves (d).

XPS measurements. The diffraction peaks of Au and P25 were marked both in Fig. 2a, peaks at 38.4° , 44° , 64.5° , and 78° were ascribed to the Au [111], [200], [220], and [311] as showed in JCPDF: 04-0784. The typical peaks resulting from the rutile phase (JCPDF: 21-1276) and anatase phase (JCPDF: 21-1272) were also labeled using different signs. Furthermore, the weak peaks from Au could be attributed to the overlapping of P25 phase, as well as the relative low loading amounts of Au. The full spectrum of XPS in Fig. 2b showed that there were elements of Au, Ti and O presented. Fig. 2c-d showed the survey spectrum of Ti2p, and Au4f in both Au-P25 and P25. As seen in Fig. 2c, there were two typical peaks which were located at 458.98 eV for Ti2p_{3/2} and 464.69 eV for Ti2p_{1/2} in pure P25 [42,43], the separated binding energy of such two peaks is 5.71 eV corresponding to the Ti⁴⁺ in oxide states [43]. The slight blue-shift of these peaks were observed in Au-P25 with 458.68 eV for Ti2p_{3/2} and 464.39 eV for Ti2p_{1/2}. Such difference could be ascribed to the forming of Ti-O-Au bond with the reduction of Au³⁺ to Au⁰. Besides, there were two peaks in Au4f spectra including Au4f_{7/2} at 83.38 eV and Au4f_{5/2} at 86.98 eV (Fig. 2d). Compared to free metallic Au (83.78 eV) [22], this indicated that the efficient charges transporting was achieved from P25 to Au and thus also confirms a strong interaction between them.

The activity of heterostructures prepared by volume variations of ethanol in diphasic system were studied in Fig. 3a-b. Au-P25 with 1% ethanol showed the best efficiency ($\sim 40\%$) compared to other ones. Au-P25 with 100% ethanol has the same activity compared to that of pure P25, and the decrease in activity could be attributed to the aggregation and irregular shape which have given rise to recombination centers of

generated electrons and thus negative results presented in catalytic efficiency [44]. This difference was also verified in the measurements of photocurrents curves in Fig. 3b, in which the photocurrents density of Au-P25 with 1% ethanol was ~ 5 times higher than that in pure P25 and was also the best ones among all heterostructure photocatalysts. IPCE measurement of bare P25 and Au-P25 with 1% ethanol was carried out to further elucidate the role of the plasmonic Au NPs in enhancing the photoactivity of P25. IPCE values were calculated based on the following equation [45]:

$$\text{IPCE}(\%) = \frac{I_{\text{ph}}(\frac{\text{mA}}{\text{cm}^2})}{J_{\text{mono}}(\frac{\text{mW}}{\text{cm}^2})} \times \frac{1240}{\lambda(\text{nm})} \times 100$$

Where I_{ph} is the measured photocurrent density, J_{mono} is the measured monochromated light power density, and λ is the incident light wavelength. Fig. 3c showed typical features, including: 1) Compared to P25, Au-P25 showed significant improvement of photoresponse at the visible range, suggesting the enhancement of photocurrent due to effective separation of charges at the interface of Au and P25 mediated by plasmon effects. 2) Au-P25 showed the highest values at $\sim 550 \text{ nm}$ in the visible region, which was matched well with the Au SPR peaks, and such a result also demonstrated that the photoactivity at visible-light range was dominated by SPR adsorption. EIS measurements were conducted to investigate the charges transfer for P25 and Au-P25 with 1% ethanol in the dark and under visible light ($\lambda > 400 \text{ nm}$). As seen in Fig. 3d, in dark conditions, the Nyquist plots for both P25 and Au-P25 exhibited large charge transfer resistance (R_{CT}), indicating negligible photocatalytic

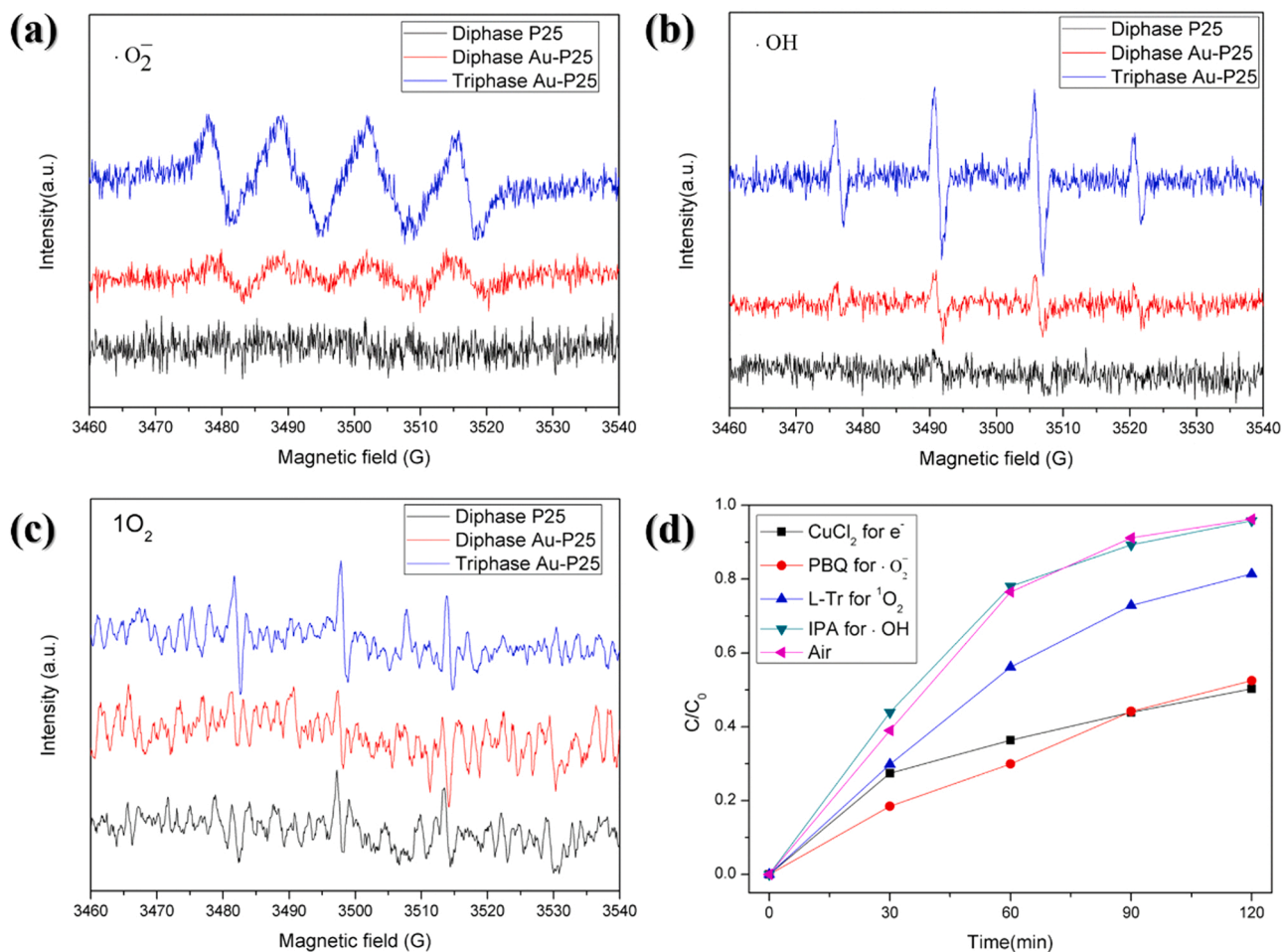


Fig. 6. EPR results of diphase P25, diphase Au-P25 and triphase Au-P25 measured at $\lambda > 400$ nm after 5 min illumination for (a) Superoxide radical ($\cdot\text{O}_2^-$), (b) hydroxide radical ($\cdot\text{OH}$) and (c) singlet oxygen ($^1\text{O}_2$). (d) Corresponding scavenger experiments of photocatalytic SA degradation for the PMSHs mediated system.

activity without light illumination. R_{CT} of Au-P25 was much lower than that of bare P25, and this could be attributed to the change of electrical performance after Au elements doping [46]. In contrast, under visible light illumination, both P25 and Au-P25 exhibited smaller R_{CT} , especially for Au-P25 there was a dramatic decrease of resistance, suggesting the excellent performance for charges transfer with the help of plasmon effects. Meanwhile, the slight lower of R_{CT} for P25 under visible light illumination might be regarded as residual UV light from filters which then activated P25.

3.2. Studies of photoactivity by constructing triphase system

The triphase based photocatalytic membrane was characterized by SEM and measurement of water contact angle in Fig. 4. Specifically, P25 or Au-P25 was located on the surface of superhydrophobic carbon black membrane with a help of a filtering process by dropping the mixture solution of photocatalysts, followed by a post-heating process. As shown of cross-section image (Fig. 4a), it could be estimated that the thickness of coated Au-P25 or P25 was $1.1 \pm 0.5 \mu\text{m}$, which well-matched the mapping result of X-ray spectroscopy by detecting the Ti elements in P25 and C elements in carbon black (Fig. 4b), respectively. Enlarged SEM images in Fig. 4c-d also showed such difference at the microscale, the water contact angle (CA) in pure carbon black was $165 \pm 1^\circ$ due to lower surface energy mediated by modifying of PTFE on the carbon black. A reverse of CA was observed when introducing the hydrophilic photocatalysts, the CA could reach $11 \pm 1^\circ$ due to the large amounts of water-friendly groups binding on the surface of photocatalysts. Thus, the

area of superhydrophilic was used to contact and degrade with pollutants in water. Meanwhile, the air stored at the pores of the superhydrophobic area could transport O_2 at the interface of solid-liquid and then promote the generation of ROS in pollutants water.

The further improvement in catalytic activity was applied by triphase system. As seen in Fig. 5a, the increase of efficiency significantly in all samples except for P25 were observed due to the optimized reaction routes. The efficiency of SA degradation could reach $\sim 80\%$ which was ~ 2 times higher in the best ones in diphase system. Especially, the activity of Au-P25 with 100% ethanol which showed similar degradation efficiency with P25 in diphase system was improved to ~ 4 times than that in diphase, and this jumps in efficiency may be ascribed to the increasing separation capacity of electron-hole pairs and suppression of recombination due to uncontrollable transportation of electrons resulting from disordered morphology of Au NPs. Furthermore, there were no apparent difference of P25 in both systems due to their low activity in visible range. The statistic histogram in Fig. 5b also presented such differences visually, the several times increase in efficiency were observed in all PMSHs due to plasmon effects stimulated by visible light. The comparison was also showed by using Au-P25 with 1% ethanol which had the highest activity in diphase system in Fig. 5c-d. ~ 3 times and ~ 60 times increase in PMSHs combining with triphase system compared with Au-P25 with 1% ethanol in diphase system and P25 in both systems. Such result demonstrated that both optimize of PMSHs and design of reaction interface made important contributions in increase of catalytic efficiency.

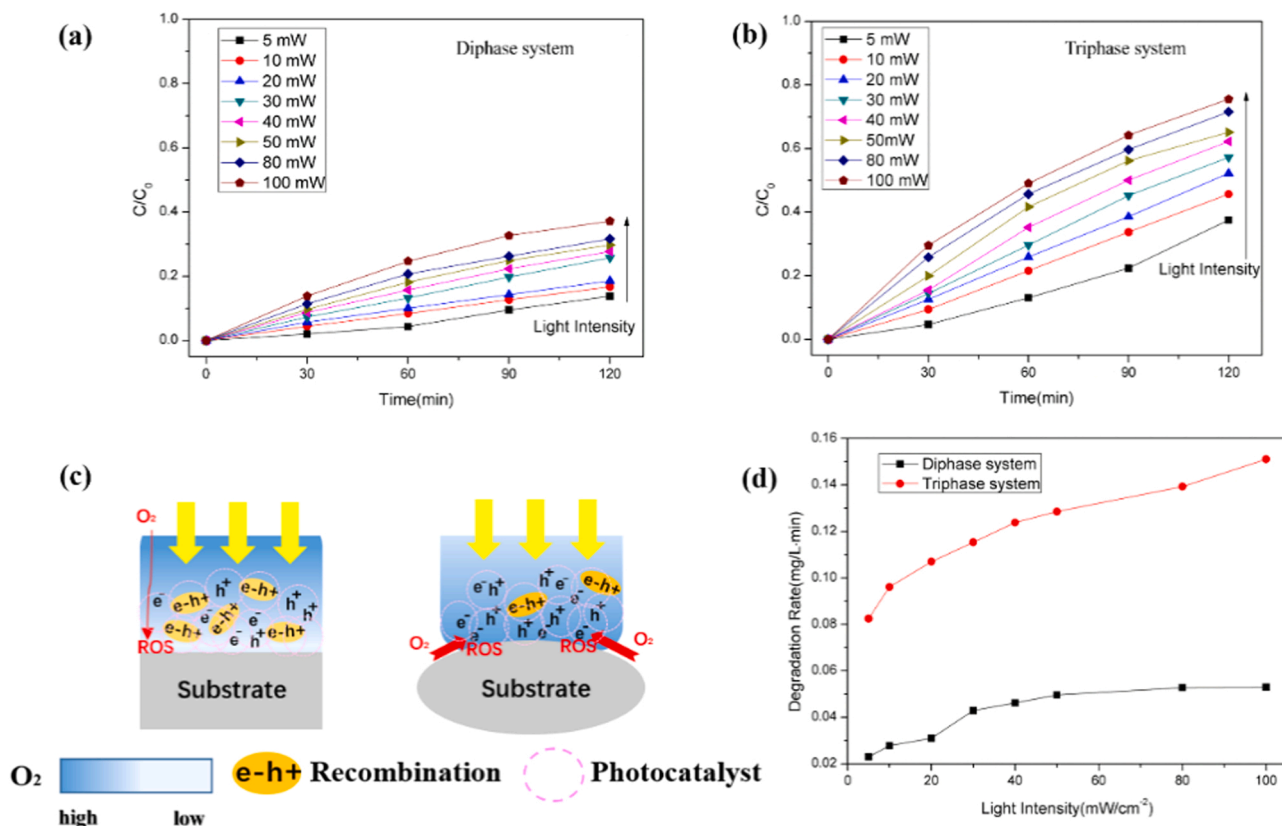


Fig. 7. Photocatalytic degradation of SA in diphasic (a) and triphasic (b) system with different light-density (5, 10, 20, 30, 40, 50, 80, 100 mW/cm²) exposure. The mechanism explanation of differences (c) and curves of degradation rates versus light density (d) in both system.

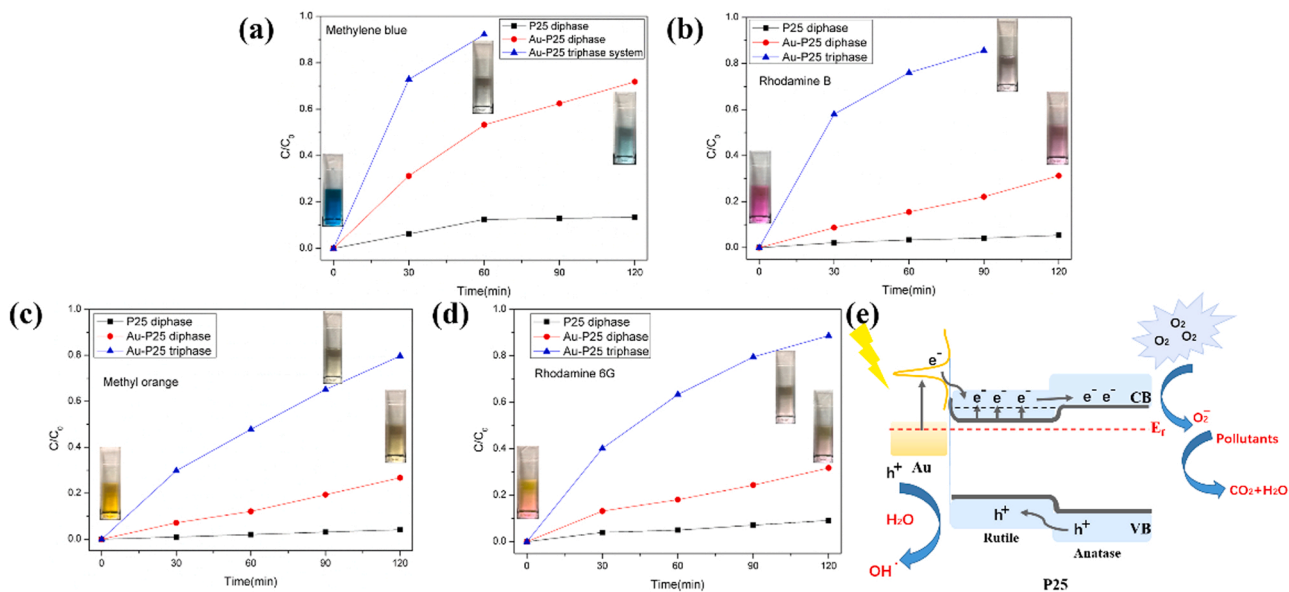
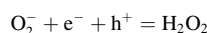
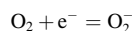
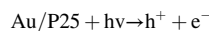
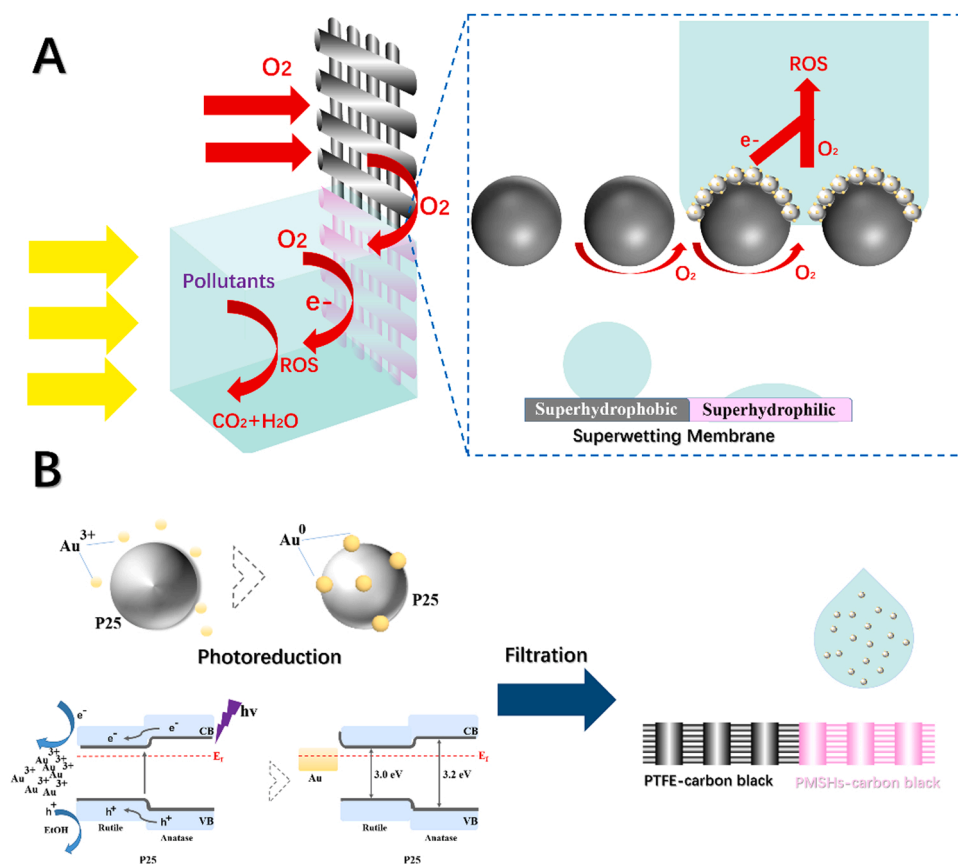


Fig. 8. Degradation of MB (a), RhB (b), MO (c) and R6G (d) under AM 1.5 simulated sunlight illumination cut off UV light. Inserts in panels a-d present the initial color of the dyes, and the color of the dyes after photocatalytic reaction based on diphasic and triphasic systems. (e) General mechanism for plasmon-mediated photocatalysis based on solid-liquid-gas triphase system.

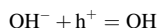
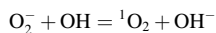
3.3. Analyses of photocatalytic enhancement in triphase system

Photo-generated ROS, including hydrogen peroxide (H_2O_2), superoxide radical ($\cdot O_2^-$), hydroxide radical ($\cdot OH$) and singlet oxygen (1O_2) are responsible for pollutants removal. The typical process was presented as follows:





Scheme 1. Schematic illustration of plasmon-mediated solid-liquid-gas triphase photocatalytic system.



Electron spin resonance (EPR) measurements were conducted to investigate ROS generated in the above proposed photocatalytic systems. DMPO methanol solution, DMPO aqueous solution, and TEMP were used as agents for $\cdot\text{O}_2^-$, $\cdot\text{OH}$ and ${}^1\text{O}_2$ trapping under visible light illumination, respectively [24,47]. As shown in Fig. 6a, peaks with relative intensities of 1:1:1:1 were ascribed to the formation of $\cdot\text{O}_2^-$ in the system, and the typical peaks intensity in triphase Au-P25 showed near 3.5 times higher than that in diphasic Au-P25. Meanwhile, the amounts of generated $\cdot\text{OH}$ which showed four characteristic peaks with relative intensities of 1:2:2:1 in triphase Au-P25 exhibited almost 3 times higher than that in diphasic Au-P25 (Fig. 6b). In addition, intermediate product of ${}^1\text{O}_2$ was also demonstrated to present (Fig. 6c) and an intensity increase of ${}^1\text{O}_2$ with a typical triplet spectrum in triphase Au-P25 was observed clearly compared to other two ones with negligible signals. Besides, to describe generated H_2O_2 , Ghormley triiodide method [48] was used for quantitatively study. Fig. S6 illustrated the amounts of generated H_2O_2 in diphasic Au-P25 and triphase Au-P25 under visible light illumination. Such high H_2O_2 generation might be ascribed as abundant interfacial O_2 involving such a process, as well as the effective suppression of recombination for charges. All these results verified that PMSHs mediated triphase systems were favorable for the ROS generation in the photocatalytic process. The fundamental role of ROS was studied further to reveal the basic degradation process. CuCl_2 , p-Benzoquinone (PBQ), L-Tryptophan (L-Tr) and isopropyl alcohol (IPA) were typical scavengers used for the detection of electrons (e^-), superoxide radical ($\cdot\text{O}_2^-$), singlet oxygen (${}^1\text{O}_2$) and hydroxide radical ($\cdot\text{OH}$), respectively. As seen in Fig. 6d, after irradiation for 120 min, there was a remarkably suppression of SA degradation after adding CuCl_2 , PBQ and

L-Tr, the degradation efficiencies were decreased to 50.32%, and 52.50% and 81.40%, respectively. Which indicated that e^- , O_2^- as well as ${}^1\text{O}_2$ were mainly responsible for SA degradation. In contrast, there was a negligible change after the addition of IPA, suggesting that $\cdot\text{OH}$ were not involved in this degradation process.

The role of dissolved oxygen was studied under different light density. As shown in Fig. 7a-b, under the lower light density (below $40 \text{ mW}/\text{cm}^2$), the linear tendency could be observed both in this two systems. But once increasing the light density over $40 \text{ mW}/\text{cm}^2$, the rates of degradation in solid-liquid system were slowed down and tend to saturation with longer time. However, the rates of degradation in solid-liquid-gas system were in susceptible maintained linearly even under higher light density (up to $100 \text{ mW}/\text{cm}^2$). Fig. 7c explained such differences presented in both systems. In solid-liquid system, the longer transporting distance of oxygen made it could not keep pace with the consuming rates of that which have been reacted with large amounts of electron-hole pairs generated within a short time. But this would step by step in solid-liquid-gas system due to their direct oxygen transporting channels at the interface between solid photocatalysts and pollutants water, which shorten the time for dissolution of oxygen and the consumed oxygen could be supplied constantly with porous superhydrophobic membrane. The comparison in Fig. 7d was also verified that the balance between supplied oxygen and consumed oxygen would raise upper-limits in degradation rates. This would bring new ideas for design of reliable photocatalytic system which work normally under the case of high-light density and thus broaden the range of applications.

The PMSHs-mediated triphase system was also applied to degrade series of organic dyes including Methylene blue (MB), rhodamine B (RhB), methyl orange (MO) and rhodamine 6 G (R6G). As shown in Fig. 8a, $\sim 90\%$ MB was degraded with Au-P25 combined with triphase system after 60 min exposure while $\sim 50\%$ MB was degraded with Au-P25 based diphasic system at the same condition. The similar trends

were also observed apparently with RhB, MO and R6G (Fig. 8b-d). The rates of degradation in all dyes were remarkably increased in PMSHs triphase system compared to that in diphasic system except for P25 based diphasic system with negligible photoactivity in visible region though there were differences of degradation rates due to intrinsic properties of dyes [47]. The general process in PMSHs mediated triphase photocatalytic system was attributed as followings in Fig. 8e: under irradiation of visible light, the excited SPR in Au NPs produced hot-electrons through non-radiative transition. Hot-electrons with energies higher than the energy of Schottky barrier then got across the interface and were injected into adjacent conduction band of rutile phase of P25. Next, the accumulation of electrons made negative shift for conduction band of rutile phase and then transferred to well-conjugated anatase phase though thermodynamically unfavorable owing to much positive position of conduction band in rutile phase (-0.05 V vs NHE) than that in anatase phase (-0.25 V) [41,49,50]. Especially, in triphase system, the adequate contents of O_2 in surroundings and shorten of O_2 transporting channels at active interface made it in great balance of supply and consumption of ROS, which further promoted the rates of redox reaction.

4. Conclusion

In summary, we have proposed a solid-liquid-gas triphase photocatalytic system combining with visible-light responding plasmonic Au-P25. Au-P25 were prepared with controllable morphology with the help of ethanol as a hole scavenger and were optimized by photocatalytic process and photocurrent measurements. The plasmon effects and Schottky interface made adsorption of visible light and effective separation of generated electron-hole pairs come into possible. Secondly, a triphase photocatalytic system combining with superhydrophobic carbon black and superhydrophilic Au-P25 was proposed for achieving optimized O_2 transporting channels, this special construction made the ROS be generated at a high rate of speed due to fast injection of interfacial O_2 . Such interface engineering for both photocatalysts and reaction system realized remarkably increase in organic pollutants degradation, SA was decomposed effectively which was ~ 3 times and ~ 60 times higher than solid-liquid diphasic system including Au-P25 and P25, respectively. The results with different light density and adjustment of dissolved oxygen were also demonstrated the crucial role of oxygen contents and the necessity for building up triphase system. Meanwhile, they also showed their wide applicability for other organic dyes degradation and superior photostability after tens of cycles. All these provide a potential approach for the future research of photocatalytic materials and application system. [Scheme 1](#).

CRediT authorship contribution statement

Shan-Jiang Wang: Conceptualization, Methodology, Investigation, Writing – original draft. **Xiao-Yang Zhang:** Validation, Writing – review & editing. **Dan Su:** Resources Visualization, Writing – review & editing. **Xi Yan:** Methodology, Writing – original draft, Investigation. **Huan-Li Zhou:** Methodology, Formal analysis. **Xiao-Mei Xue:** Resources, Investigation. **Yun-Fan Wang:** Visualization, Writing – original draft. **Tong Zhang:** Conceptualization, Supervision, Funding acquisition.

Declaration of Competing Interest

The authors declare that they have no known competing financial interests or personal relationships that could have appeared to influence the work reported in this paper.

Acknowledgments

This work is supported by MOST under Grant Number 2017YFA0205800, NSFC under grant numbers 61875241, 11734005.

Appendix A. Supporting information

Supplementary data associated with this article can be found in the online version at [doi:10.1016/j.apcatb.2022.121102](https://doi.org/10.1016/j.apcatb.2022.121102).

References

- [1] M.A. Shannon, P.W. Bonn, M. Elimelech, J.G. Georgiadis, B.J. Marinas, A. M. Mayes, Science and technology for water purification in the coming decades, *Nature* 452 (2008) 301–310.
- [2] P. Alvarez, C.K. Chan, M. Elimelech, N.J. Halas, D. Villagrán, Emerging opportunities for nanotechnology to enhance water security, *Nat. Nanotechnol.* 13 (2018) 8–641.
- [3] M.R. Hoffmann, S.T. Martin, W. Choi, D.W. Bahnemann, Environmental applications of semiconductor photocatalysis, *Chem. Rev.* 95 (1995) 69–96.
- [4] S. Malato, P. Fernández-Ibáñez, M.I. Maldonado, J. Blanco, W. Gernjak, Decontamination and disinfection of water by solar photocatalysis: recent overview and trends, *Catal. Today* 147 (2009) 1–59.
- [5] B.C. Hodges, E.L. Cates, K. Jae-Hong, Challenges and prospects of advanced oxidation water treatment processes using catalytic nanomaterials, *Nat. Nanotechnol.* 13 (2018) 642–650.
- [6] A.L. Linsebigler, G. Lu, J.T. Yates, Photocatalysis on TiO_2 Surfaces: Principles, Mechanisms, and Selected Results, *Chem. Rev.* 95 (1995) 735–758.
- [7] L. Vayssieres, Growth of arrayed nanorods and nanowires of ZnO from aqueous solutions, *Adv. Mater.* 15 (2010) 464–466.
- [8] L. Gao, J. Zhuang, L. Nie, J. Zhang, Y. Zhang, N. Gu, T. Wang, J. Feng, D. Yang, S. Perrett, Intrinsic peroxidase-like activity of ferromagnetic nanoparticles, *Nat. Nanotech.* 2 (2007) 577–583.
- [9] V. Etacheri, M.K. Seery, S.J. Hinder, S.C. Pillai, Highly visible light active TiO_2 -xNx heterojunction photocatalysts, *Chem. Mater.* 22 (2010) 3843–3853.
- [10] N. Wetchakun, S. Chaiwichain, B. Inceesungvorn, K. Pingmuang, S. Phanichphant, A.I. Minett, J. Chen, $BiVO_4/CeO_2$ nanocomposites with high visible-light-induced photocatalytic activity, *ACS Appl. Mater. Interfaces* 4 (2012), 3718–23.
- [11] J.Y. Park, L.R. Baker, G.A. Somorjai, Role of hot electrons and metal-oxide interfaces in surface chemistry and catalytic reactions, *Chem. Rev.* 115 (2015) 2781–2817.
- [12] S.N. Reddy Inturi, T. Boningari, M. Suidan, P.G. Smirniotis, Visible-light-induced photodegradation of gas phase acetonitrile using aerosol-made transition metal (V, Cr, Fe, Co, Mn, Mo, Ni, Cu, Y, Ce, and Zr) doped TiO_2 , *Appl. Catal. B-Environ.* 144 (2014) 333–342.
- [13] J. Reszczyńska, T. Grzyb, J.W. Sobczak, W. Lisowski, M. Gazda, B. Ohtani, A. Zaleski, Visible light activity of rare earth metal doped (Er^{3+} , Yb^{3+} or Er^{3+}/Yb^{3+}) titania photocatalysts, *Appl. Catal. B-Environ.* 163 (2015) 40–49.
- [14] J. Fang, X. Lin, Z. Zhang, Y. Yuan, C. Xue, Au@ TiO_2 -CdS ternary nanostructures for efficient visible-light-driven hydrogen generation, *ACS Appl. Mater. Interfaces* 5 (2013) 16–92.
- [15] C. Freysoldt, B. Grabowski, T. Hickel, J. Neugebauer, C. Walle, First-principles calculations for point defects in solids, *Rev. Mod. Phys.* 86 (2014) 1–305.
- [16] U. Aslam, V.G. Rao, S. Chavez, S. Linic, Catalytic conversion of solar to chemical energy on plasmonic metal nanostructures, *Nat. Catal.* 1 (2018) 656–665.
- [17] C. Zhan, X.J. Chen, J. Yi, J.F. Li, D.Y. Wu, Z.Q. Tian, From plasmon-enhanced molecular spectroscopy to plasmon-mediated chemical reactions, *Nat. Rev. Chem.* 2 (2018) 216–230.
- [18] T. Zhang, S.J. Wang, X.Y. Zhang, D. Su, Y. Yang, J.Y. Wu, Y.Y. Xu, N. Zhao, Progress in the utilization efficiency improvement of hot carriers in plasmon-mediated heterostructure photocatalysis, *Appl. Sci.* 9 (2019) 2093.
- [19] L. Yuan, Z. Geng, J. Xu, F. Guo, C. Han, Metal-Semiconductor Heterostructures for Photoredox Catalysis: Where Are We Now and Where Do We Go? *Adv. Funct. Mater.* 31 (2021), 2101103.
- [20] S.A. Maier, M.L. Brongersma, P.G. Kik, S. Meltzer, A.A.G. Requich, H.A. Atwater, Plasmonics- A route to nanoscale optical devices, *Adv. Mater.* 13 (2001) 1501–1505.
- [21] J.A. Lopez-Sanchez, N. Dimitratos, C. Hammond, G.L. Brett, L. Kesavan, S. White, P. Miedziak, R. Tiruvalam, R.L. Jenkins, A.F. Carley, D. Knight, C.J. Kiely, G. J. Hutchings, Facile removal of stabilizer-ligands from supported gold nanoparticles, *Nat. Chem.* 3 (2011), 551–6.
- [22] D. Ding, K. Liu, S. He, C. Gao, Y. Yin, Ligand-exchange assisted formation of Au/ TiO_2 Schottky contact for visible-light photocatalysis, *Nano Lett.* 14 (2014), 6731–6.
- [23] K.S. Leschkes, R. Divakar, J. Basu, E. Enache-Pommer, J.E. Boercker, C.B. Carter, U.R. Kortshagen, D.J. Norris, E.S. Aydil, Photosensitization of ZnO nanowires with CdSe quantum dots for photovoltaic devices, *Nano Lett.* 7 (2007), 1793–8.
- [24] W. He, H.K. Kim, W.G. Warner, D. Melka, J.H. Ca Lahan, J.J. Yin, Photogenerated charge carriers and reactive oxygen species in ZnO/Au hybrid nanostructures with enhanced photocatalytic and antibacterial activity, *J. Am. Chem. Soc.* 136 (2014) 750–757.
- [25] J. Fernando, M.P. Shortell, C.J. Noble, J.R. Harmer, E.A. Jaatinen, E.R. Waclawik, Controlling Au photodeposition on large ZnO nanoparticles, *ACS Appl. Mater. Interfaces* 8 (2016) 14271–14283.
- [26] M.E. Aguirre, G. Custo, M.S. Goes, P.R. Bueno, G. Zampieri, M.A. Grela, Critical water effect on the plasmon band and visible light activity of Au/ZnO nanocomposites, *J. Phys. Chem. C* 118 (2014) 2018–2027.
- [27] A. Mh, C. Mhb, Photocatalytic performance of aerogels for organic dyes removal from wastewaters: review study, *J. Mol. Liq.* (2020) 309.

- [28] M. Tahir, S. Tasleem, B. Tahir, Recent development in band engineering of binary semiconductor materials for solar driven photocatalytic hydrogen production, *Int. J. Hydrog. Energy* 45 (2020) 15985–16038.
- [29] L. Wu, A.C. Sedgwick, X. Sun, S.D. Bull, T.D. James, Reaction-based fluorescent probes for the detection and imaging of reactive oxygen, nitrogen, and sulfur species, *Acc. Chem. Res.* 52 (2019) 2582–2597.
- [30] D.D. Dionysiou, A.A. Burbano, M.T. SuiDan, I. Baudin, J.M. Laíné, Effect of oxygen in a thin-film rotating disk photocatalytic reactor, *Environ. Sci. Technol.* 36 (2002) 3834–3843.
- [31] M.H. Zarifi, S. Farsinezhad, M. Abdolrazzaghi, M. Daneshmand, K. Shankar, Selective microwave sensors exploiting the interaction of analytes with trap states in TiO₂ nanotube arrays, *Nanoscale* 8 (2016) 7466–7473.
- [32] X. Xiong, Z. Wang, Y. Zhang, Z. Li, R. Shi, T. Zhang, Wettability controlled photocatalytic reactive oxygen generation and *Klebsiella pneumoniae* inactivation over triphase systems, *Appl. Catal. B-Environ.* 264 (2020), 118518.
- [33] X. Sheng, Z. Liu, R. Zeng, L. Chen, X. Feng, L. Jiang, Enhanced photocatalytic reaction at air-liquid-solid joint interfaces, *J. Am. Chem. Soc.* 139 (2017) 12402–12405.
- [34] R. Shi, L. Shang, T. Zhang, Three phase interface engineering for advanced catalytic applications, *ACS Appl. Energy Mater.* 4 (2021) 1045–1052.
- [35] L. Chen, X. Feng, Enhanced catalytic reaction at an air-liquid-solid triphase interface, *Chem. Sci.* 11 (2020) 3124–3131.
- [36] H. Zhou, X. Sheng, J. Xiao, Z. Ding, D. Wang, X. Zhang, J. Liu, R. Wu, X. Feng, L. Jiang, Increasing the efficiency of photocatalytic reactions via surface microenvironment engineering, *J. Am. Chem. Soc.* 142 (2020) 2738–2743.
- [37] Y. Gao, N. Yang, S. Lu, T. You, P. Yin, In situ monitoring of plasmon-driven photocatalytic reactions at gas-liquid-solid three-phase interfaces by surface-enhanced Raman spectroscopy, *J. Mater. Chem. C* 7 (2019), 9926–4098.
- [38] D. Wang, L. Chen, J. Liu, F. Guan, R. Sun, L. Jiang, X. Feng, A reliable photoelectrochemical bioassay system based on cathodic reaction at a solid-liquid-air joint interface, *Adv. Funct. Mater.* 28 (2018), 1804410.
- [39] J. Li, G. Chen, Y. Zhu, Z. Liang, A. Pei, C.L. Wu, H. Wang, H.R. Lee, K. Liu, S. Chu, Y. Cui, Efficient electrocatalytic CO₂ reduction on a three-phase interface, *Nat. Catal.* 1 (2018) 592–600.
- [40] Y. Li, Y. Guo, R. Long, D. Liu, D. Zhao, Y. Tan, C. Gao, S. Shen, Y. Xiong, Steering plasmonic hot electrons to realize enhanced full-spectrum photocatalytic hydrogen evolution, *Chinese, J. Catal.* 39 (2018) 453–462.
- [41] D. Tsukamoto, Y. Shiraishi, Y. Sugano, S. Ichikawa, S. Tanaka, T. Hirai, Gold nanoparticles located at the interface of anatase/rutile TiO₂ particles as active plasmonic photocatalysts for aerobic oxidation, *J. Am. Chem. Soc.* 134 (2012) 6309–6315.
- [42] K. Shoueir, S. Kandil, H. El-hosainy, M. El-Kemary, Tailoring the surface reactivity of plasmonic Au@TiO₂ photocatalyst bio-based chitosan fiber towards cleaner of harmful water pollutants under visible-light irradiation, *J. Clean. Prod.* 230 (2019) 383e393–393.
- [43] K. Safeen, V. Micheli, R. Bartali, G. Gottard, N. Laidani, Low temperature growth study of nano-crystalline TiO₂ thin films deposited by RF sputtering, *J. Phys. D: Appl. Phys.* 48 (2015), 295201.
- [44] S. Bai, W. Jiang, Z. Li, Y. Xiong, Surface and interface engineering in photocatalysis, *ChemNanoMat* 1 (2015) 223–239.
- [45] Y.C. Pu, G. Wang, K.D. Chang, Y. Ling, Y.K. Lin, B.C. Fitzmorris, C.M. Liu, X. Lu, Y. Tong, J.Z. Zhang, Y.J. Hsu, Y. Li, Au nanostructure-decorated TiO₂ nanowires exhibiting photoactivity across entire UV–visible region for photoelectrochemical water splitting, *Nano Lett.* 13 (2013) 3817–3823.
- [46] S.F. Hung, F.X. Xiao, Y.Y. Hsu, N.T. Suen, H.B. Yang, H.M. Chen, B. Liu, Iridium oxide-assisted plasmon-induced hot carriers: improvement on kinetics and thermodynamics of hot carriers, *Adv. Energy Mater.* 6 (2016), 1501339.
- [47] Y. Duan, J. Luo, S. Zhou, X. Mao, M.W. Shah, F. Wang, Z. Chen, C. Wang, TiO₂-supported Ag nanoclusters with enhanced visible light activity for the photocatalytic removal of NO, *Appl. Catal. B-Environ.* 234 (2018) 206–212.
- [48] V. Diesen, M. Jonsson, Formation of H₂O₂ in TiO₂ photocatalysis of oxygenated and deoxygenated aqueous systems: a probe for photocatalytically produced hydroxyl radicals, *J. Phys. Chem. C* 118 (2014) 10083–10087.
- [49] D. Zhang, M. Yang, S. Dong, D.O. Scanlon, Electric-dipole effect of defects on the energy band alignment of rutile and anatase TiO₂, *Phys. Chem. Chem. Phys.* 17 (2015), 29079–84.
- [50] T. Kawahara, Y. Konishi, H. Tada, N. Tohge, J. Nishii, S. Ito, A patterned TiO₂ (Anatase)/TiO₂ (Rutile) bilayer-type photocatalyst: effect of the anatase/rutile junction on the photocatalytic activity, *Angew. Chem. Int. Ed.* 41 (2002) 2811–2813.